Title

Achieving large area exfoliation in 128Y-cut lithium niobate

Author

Ravi, Nishanth

Publication Date

2024

Peer reviewed|Thesis/dissertation

UNIVERSITY OF CALIFORNIA

Los Angeles

Achieving large area exfoliation in 128Y-cut lithium niobate

A thesis submitted in partial satisfaction

of the requirements for the degree Master of Science

in Materials Science and Engineering

by

Nishanth Ravi

2024

ABSTRACT OF THE THESIS

Achieving large area exfoliation in 128Y-cut lithium niobate

by

Nishanth Ravi

Master of Materials Science and Engineering

University of California, Los Angeles, 2024

Professor Mark S. Goorsky, Chair

This study investigates the mechanisms of helium implantation induced blistering and exfoliation in lithium niobate ($LiNbO_3$). Wafers of $LiNbO_3$ were implanted to a dose of 2.3×10^{16} He^+/cm^2 and an accelerating voltage of 250 keV. The wafer was cooled such that it remained at room temperature during the implantation to limit helium diffusion or bubble growth due to the heating caused by the ion implantation process. The implant profile and exfoliation behavior of the samples for various annealing recipes were investigated using high resolution X-Ray diffraction (HRXRD), optical microscopy and contact profilometry. It was found that a low temperature "defect nucleation" anneal at 120 ˚C followed by a high temperature "bubble growth"

anneal at 200 ˚C caused millimeter-scale large-area exfoliation of thin-film lithium niobate with a thickness of 800 nm, which is the projected range of the helium ion implantation done at 250 keV. In comparison, a single anneal at 200 ˚C caused μm-scale small-area exfoliation also referred to as blistering [1]. Large-area exfoliation is preferred over blistering, as it facilitates the next processing step of chemical mechanical polishing (CMP). Also, the long low temperature annealing improves the interfacial bond strength of the bonded wafers in the “Smart Cut” technique.

The thesis of Nishanth Ravi is approved.

Jaime Marian

Yang Yang

Mark S. Goorsky, Committee Chair

University of California, Los Angeles

2024

Table of Contents

List of Figures

List of Tables

ACKNOWLEDGEMENTS

Firstly, I would like to thank my advisor Dr. Mark Goorsky, who inculcated my interest in research. Since I joined the group in January 2023 with no prior experience, all the research ideologies I have learnt so far has been through interactions I have had with him. I strive to be as knowledgeable as him one day. I look forward to working with him as I continue my Doctoral studies under his guidance.

My mother, father, brother and sister-in-law have been a constant support system during my stay in the US so far and have helped me focus on my research. I look forward to the daily video calls I have with my parents to discuss my research work.

I would also like to thank my teammates at the Electronic Materials Group, for their support. I greatly value the conversations I had with Michael Liao and Lezli Matto who helped me start work in the group and were crucial in formulating the hypothesis of this work. I also appreciate Brandon Carson's help with learning X-Ray diffraction and the various measurements that could be done using the technique when I first started working in the group. Most of the content in this thesis related to the XRD strain fringes were from my discussions with him.

Lastly, I would like to thank all my friends who have also been my support system since I first landed in LA.

CHAPTER 1: INTRODUCTION

Lithium niobate (LiNbO3, trigonal) has emerged as a significant material in the fields of photonics and acoustics due to its ferroelectric, piezoelectric, and nonlinear optical capabilities. These properties make lithium niobate valuable in surface acoustic wave (SAW) filters and thin-film bulk acoustic resonators (FBAR). These devices utilize the piezoelectric properties of thin-film lithium niobate for use in high-frequency RF filtering applications.

Due to its precision in filtering, delaying, and transducing signals, SAW devices are immensely helpful in the design of modern communication systems, particularly in the quickly expanding field of wireless communications. The enhanced efficiency of SAW filters and resonators is attributed to their fast acoustic velocity and reduced propagation loss. Furthermore, the high coupling coefficient of the material increases the acoustic wave transduction process efficiency, allowing for the creation of devices with better functionality and sensitivity. Beyond conventional SAW and FBAR applications, lithium niobate finds use in quantum computing, optomechanics, and sensor technologies.

Lithium niobate has a trigonal structure with an in-plane lattice parameter of 5.15 Å and an out-of-plane lattice parameter of 13.78 Å [2]. lithium niobate as a material has been a major focus for these applications in comparison to other counterparts like sapphire (Al_2O_3) and aluminum nitride (AlN) because of the following reasons:

1. Coupling coefficient: This is a quantitative way to indicate how efficiently a device (i.e. filter or resonator) can convert electrical energy into mechanical energy and vice versa. A higher coupling coefficient allows for better control and conversion of RF signals, leading to more efficient and effective filters. The higher coupling coefficient of lithium niobate

leads to improved performance which leads to a wider bandwidth of the devices and higher slope which allows faster transition from pass to stop as the frequency varies. Wider bandwidth offered by lithium niobate-based devices are beneficial in modern communication systems that require broad frequency ranges to accommodate the increasing demand for data transmission. Wider bandwidth enables filters that can support multiple frequencies within the same device, making them ideal for multi-band and multi-mode applications.

2. Quality Factor (Q-Factor): The quality factor of a filter indicates its efficiency in filtering a specific frequency band. lithium niobate exhibits a higher Q-factor in comparison to sapphire and aluminum nitride. While this may not be crucial in low frequencies, the higher Q-factor is paramount for device performance in high frequency applications.

3. Low Insertion Loss: Insertion loss refers to the amount of signal power lost due to the insertion of a filter into the signal's path. The low insertion loss is crucial for maintaining signal strength and quality, especially in high frequency applications where signal attenuation is prevalent. This is offered by offered by lithium niobate-based devices.

4. High Temperature Stability: Stoichiometric lithium niobate (atomic ratio of Li:Nb = 1:1) does not undergo phase transformation until its melting temperature of ~ 1100 ˚C and thus retains its structure and properties. On the other hand, at ~ 900 ˚C "congruent" lithium niobate partially undergoes a phase transformation to $LiNb_3O_8$, which reduces the device performance. Here, the term "congruent composition" refers to the Li_2O concentration of 48% where it is seen that liquid lithium niobate spontaneously transforms to its solid phase. Thus, stoichiometric lithium niobate is useful in high-temperature applications and is

important for the DARPA “HOTS” project which aims to develop filters that can function at 800 ˚C for up to 30 minutes.

CHAPTER 2: BACKGROUND AND THEORY

2.1: Smartcut technique for thin-film fabrication

The end goal of this project (in collaboration with Dr. Ruochen Lu, UT Austin) is to create a thin film stack of 128Y-cut lithium niobate on sapphire. The thin film stack of lithium niobate will include up to six thin films of lithium niobate on top of each other with a twist of 180˚ between every layer. This twist helps the SAW device enhance its coupling efficiency. The first step for creating this stack would be to perform direct wafer bonding of sapphire to lithium niobate.

In this technique, wafers are bonded to each other without the use of an intermediate layer. First, the wafers undergo appropriate surface treatment. The wafers are first cleaned using an RCA (NH_4OH: H_2O_2: H_2O = 1:1:5) bath at 80 ˚C for 10 minutes. This helps remove any surface contaminants which would have reduced the bond quality. Next, hydrofluoric acid dip or oxygen plasma treatment can be used to increase the hydrophilicity of the wafers as such surfaces form stronger bonds. Direct wafer bonding relies on Van der Waals forces between atomically flat surfaces. Subsequent annealing of the bonded wafers can be used to further strengthen the bond. After bonding, the thickness of the lithium niobate wafer needs to be reduced from 500 μm to the final thickness of 40 nm-200 nm depending on the device design. The same bonding and thinning procedure will be repeated for every additional lithium niobate layer.

Thin films of materials can be fabricated by two techniques. The first approach is to perform lapping. In this technique, a rotating plate is first conditioned using the slurry and a conditioning plate. Slurries are usually alumina or silicon carbide of varying particle sizes depending on the desired removal rate. The wafers are mounted on a jig using a vacuum chuck and are placed on the rotating plate, which can be made of either metal or glass. Jig pressure, slurry

particle size and rotation speed of the rotating plate are other parameters that can be used to change the removal rate. Lapping causes subsurface damage making lapped surfaces unsuitable for devices. Hence, chemical mechanical polishing (CMP) is used to remove the damaged layers and thin down the lithium niobate film to its final thickness.

The second approach is by a technique popularized as "Smart Cut" [9] which involves exfoliation of a thin layer by ion implantation of a light ion such as hydrogen or helium. This technique involves ion implanting lithium niobate with helium ions wafers prior to direct wafer bonding. During ion implantation, energetic impurity atoms are introduced into the substrate wafer. This process often finds use in silicon semiconductor technology to dope specific regions of the wafer defined by photoresist masks. Implantation is often carried out in an ion energy range of 50 to 500 keV. At this energy, instead of sputtering the substrate atoms, the ions have enough energy to penetrate the substrate surface. For purposes of this project, helium ion implantation is used. A common ion implanter has the following components:

1) Ion Source: This contains a heated filament that converts the dopant from a gaseous or vapor phase into ions. A magnetic field perpendicular to the applied voltage is used to confine the electrons to a helical path thus increasing the probability of ionization.
2) Mass Analyzer: Depending on the gas/vapor used in the ion source, multiple ion species may be generated including contaminants like O_2^+ and C^+. The mass analyzer involves passing the ion beam through a magnetic field with a slit at the end. Only the ions with a specific mass to charge ratio would pass through the slit, which would be He^+ ions in this project.
3) Ion Acceleration Column: The mass-analyzed ions are then passed through a linear electric field which accelerates the ions to the required implant energy, i.e. 250 keV.

The accelerated beam is then rastered across the sample using a combination of perpendicular electric fields to ensure implantation uniformity across the sample surface. The concentration profile of the dopant atoms introduced by ion implantation has a skewed gaussian relationship with the depth. As atoms in a single crystal wafer are arranged in a regular pattern, if the incident ion beam is at a specific angle with respect to the crystallographic directions, they might travel for longer distances with minimal scattering. This effect is known as channeling and leads to unpredictable implant profiles. Thus, the ion beam is often oriented at an angle of 7˚ with respect to the wafer to eliminate channeling effects to improve control on the implant profile. The SRIM software [3], utilizes Monte-Carlo simulations to predict the implant profile of an ion in a substrate. The SRIM profile for a 250 keV He^+ implant in lithium niobate is shown in Fig. 1 below. It is seen that the expected peak implant concentration of 10^{21} atoms/cm^3 occurs at a depth of 796 nm also known as projected range, with a straggle of 120 nm. As discussed later in this report, during annealing of helium implanted substrates, the interstitial helium impurities segregated out of the substrate lattice depending on the segregation coefficient at the annealing temperature at the projected range to form helium gas bubbles. As annealing proceeds, the pressure in the gas bubbles increases with annealing time and at a critical point, the pressure enables crack propagation in either the in-plane or out-of-plane direction; thus, enabling the exfoliation of thin-film lithium niobate with a thickness equal to the projected range.

After ion implantation, the substrate is direct wafer bonded to a carrier wafer onto which the thin film needs to be transferred. The bonded wafer pair is then annealed. Due to their low solid solubility, the interstitial helium atoms segregate out of their lattice sites to form bubbles of helium near the projected range of the ion implant. There are two annealing regimes of helium implanted wafers. The annealing temperature has a two-fold effect on the segregation behavior of helium.

1. Size of bubbles: At low temperatures, the driving force for helium segregation is low, which promotes the formation of many small nuclei of helium, while at high temperatures, higher driving forces cause the formation of fewer and larger nuclei [4]. This is analogous to second phase strengthening where the strengthening effect caused by a high temperature anneal is less pronounced in comparison to annealing performed at lower temperatures. This occurs via the Ostwald ripening process where fine grains of the second phase coalesce to form coarser grains in order to reduce the surface energy of the second phase. The increased grain size of the second phase leads to a reduction in the dislocation pinning effect which leads to a decrease in second phase strengthening.
2. Depth of bubbles: As discussed previously the concentration profile follows a skewed gaussian distribution with respect to depth. Consider low and high annealing temperatures of T_L and T_H with corresponding helium solid solubility of S_L and S_H respectively. It is known that the Solid Solubility decreases with an increase in temperature, hence $S_L > S_H$. The SRIM simulated implant profile for the 250 keV implant is shown by the red curve in Fig. 1 below.

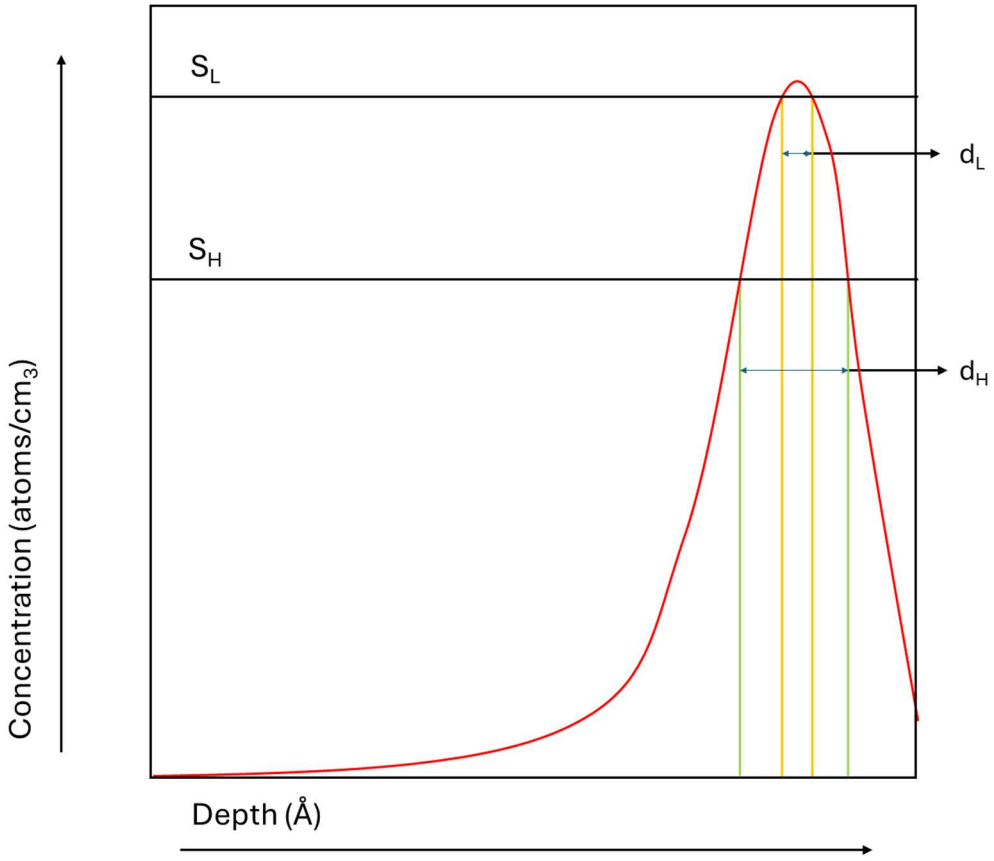

Figure 1: Concentration profile of the 250 keV helium implant in lithium niobate [3]

During annealing at a low temperature, the solid solubility S_L restricts the helium segregation to the region of thickness d_L between the two yellow lines. This is visualized in the schematic shown in Fig. 2b, helium bubbles segregated at a low temperature allow easy crack propagation during a subsequent high temperature step promoting large, exfoliated regions. Instead, if the sample was directly annealed at a high temperature, due to the lower solid solubility, the range of depth at which bubble growth occurs increases to d_H (shown by the green lines) thus reducing the control on the depth of nucleated bubbles.

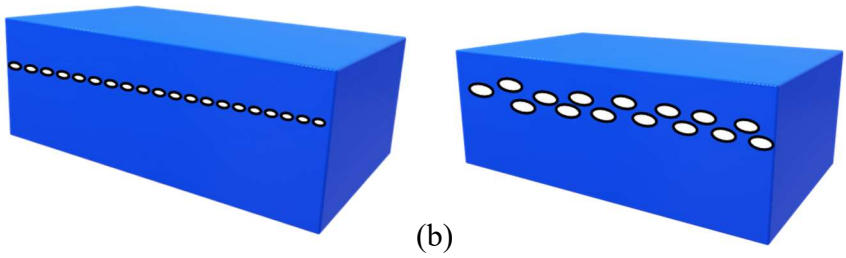

Figure 2: Schematic of bubble growth during annealing performed at (a) low temperature (b) high temperature

The two modes of exfoliation explored in this thesis are:

1. Blistering: This mode of exfoliation occurs when there is scattered helium bubble growth at a range of depths near the projected range as shown in Fig. 2b. As the helium bubbles grow, the pressure of the helium gas in the bubbles increases. At a critical point, the bubble pressure is enough to cause crack propagation in both in-plane and out-of-plane directions. This leads to exfoliation of circle shaped thin films of the implanted wafer. This is seen as circular regions visible in the optical microscope image of a blistered InP surface in Fig. 3. In the case of 128 Y-cut lithium niobate, the exfoliated regions are elliptical in shape with a size of 40-50 μm.

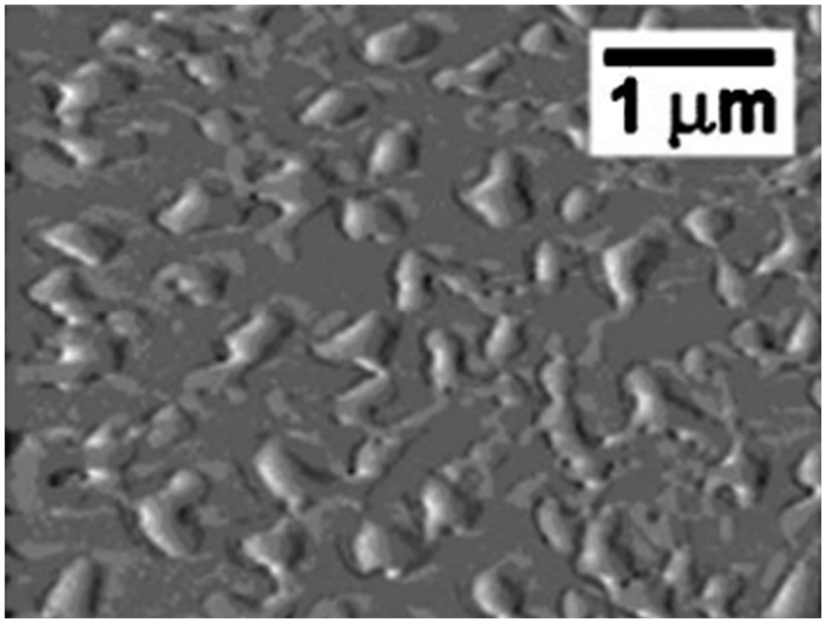

Figure 3: Exfoliation of subsurface bubble growth during blistering [4]

2. Large-area exfoliation: In this mode of exfoliation, a low temperature step is used to nucleate helium bubbles at the projected range of the implant. Further growth of the nucleated bubbles happens at the high temperature step. Due to the implant profile and bubble growth mechanics, helium nucleation at low temperatures occurs at a restricted range of depth as shown in Fig. 2a. helium bubbles grown by these two annealing steps are closer to each other and allow easy crack propagation. This leads to exfoliated regions of a larger size. The optical microscope image in Fig. 4 shows the morphology of a sample of indium phosphide after large area exfoliation.

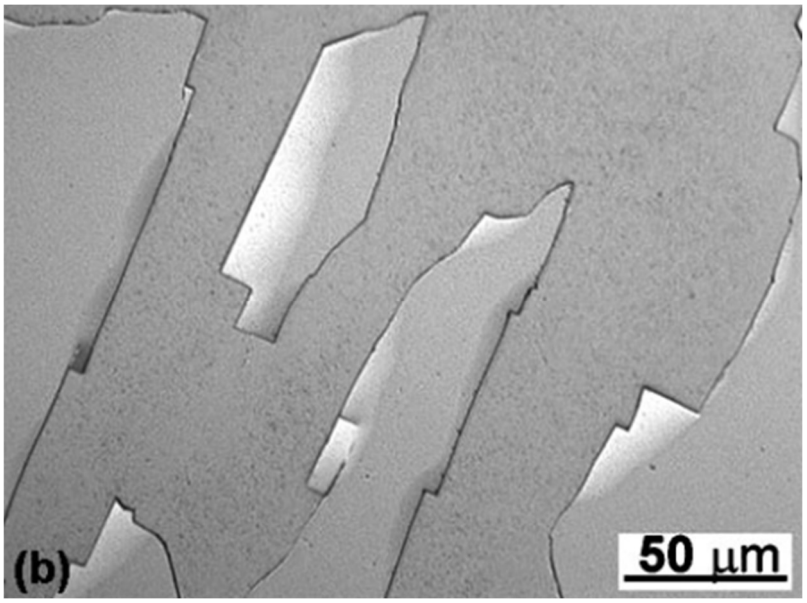

Figure 4: Optical microscope image of large area exfoliation [4]

2.2 High resolution X-Ray Diffraction (HRXRD):

X-ray diffraction is a materials characterization technique that works by utilizing the relationship between the lattice spacing (i.e., the separation of crystallographic planes) and the scattering angle also known as Bragg's law. Thompson scattering of the incident x-ray photons cause atomic planes to act like mirrors to the x-ray as shown in Fig. 5 [5]. There is a phase shift between x-rays "reflected" from the top two atomic planes in the figure, and the phase shift is calculated as $2d\sin\theta$, where d is the interatomic spacing and θ is the angle of incidence of the x-rays. If this phase shift is an integral multiple of the wavelength, constructive interference occurs. This leads to Bragg's Law:

$$\lambda = 2d \sin \theta \qquad (1)$$

Here n is the order of diffraction maxima and λ is the wavelength of the x-ray used. Hence, the angle at which constructive interference occurs can be used to predict the material, its crystal structure, composition, and strain, among other properties

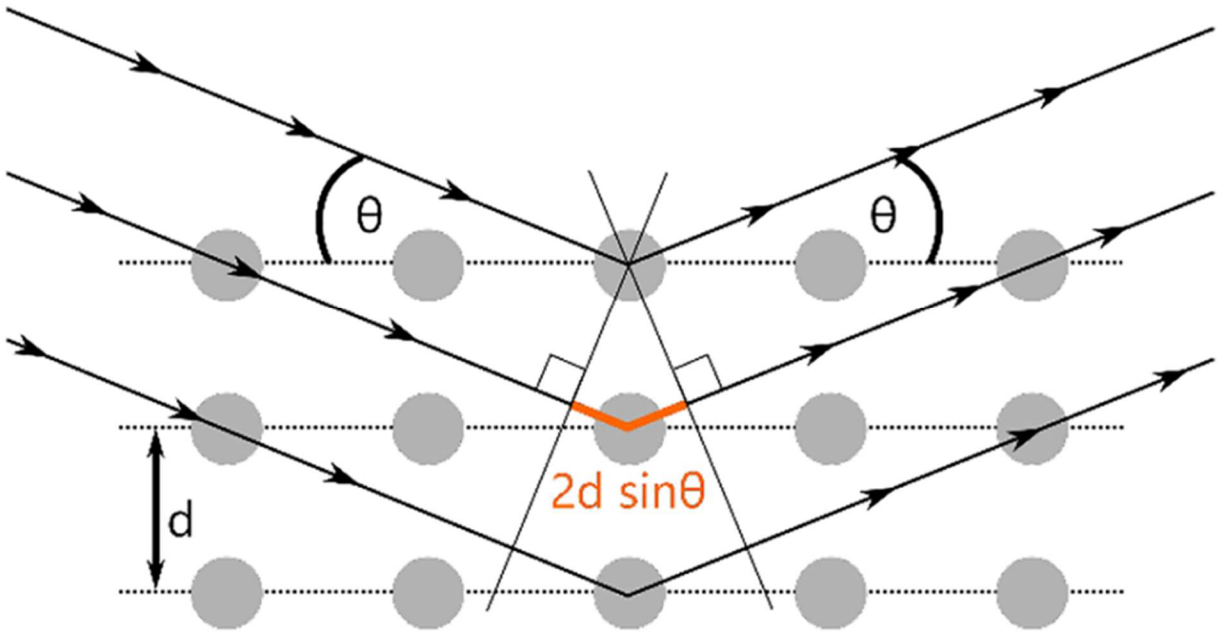

Figure 5: X-Ray scattering by atomic planes [5]

Along with HRXRD measurements, optical microscopy is also being used to capture the growth of subsurface helium bubbles and the size of the exfoliated regions with Adobe Photoshop being used to calculate the exfoliated area. Also, stylus profilometry (also known as contact profilometry) is used to confirm if the exfoliation is caused by the ion implantation and annealing procedure.

CHAPTER 3: EXPERIMENTAL

3.1: Sample information:

In this study, 3-inch 128-Y cut lithium niobate wafers were first implanted with helium ions at an energy of 250 keV and an ion dosage of $2.3x10^{16}$ ions/cm^2 [1]. The 128Y-cut orientation of lithium niobate has a surface plane of (1 0 $\bar{1}$ 4). As discussed earlier, during ion implantation, the wafer was titled at an angle of 7 degrees to avoid channeling. The ion interacts with both the substrate nuclei and electrons, referred to as nuclear stopping and electron stopping, respectively. During the implantation process, these interactions lead to an increase in the temperature of the substrate. Thus, the substrate is held at room temperature during the implantation process to minimize unwanted helium migration. Similarly, the as-implanted samples were placed in a refrigerator at 0 ˚C until the low temperature anneal was performed. After the low temperature anneal, the bubbles would have already segregated at the projected range thus helium migration at ambient temperatures would be minimal.

3.2: High Resolution XRD (HRXRD):

The XRD equipment is set up as shown in Fig. 6. The sample is mounted vertically on the stage. The detector can be rotated around the sample, using the 2θ motor. The sample itself can rotate on all three planes. The first motion is around a vertical axis using the ω motor. Similarly, motion around the horizontal axis is performed using the χ motor. Motion around the axis perpendicular to the sample surface is done by the ϕ motor but is not shown in the diagram as it wasn't used in this thesis. Additionally, the equipment has been modified to support triple axis diffraction measurements, which reduce instrumental broadening in XRD scans thus providing the resolution necessary to capture the strain fringes discussed in later in this section. The first axis is

a beam conditioner consisting of a (220) silicon monochromator. The sample stage acts as the second axis. Axis 3 is an analyzer crystal made using channel cut (220) silicon which enhances the resolution. All scans performed in this work utilize a D1 (Bruker/Jordan Valley) diffractor using Cu Kα1 radiation fitted with such a triple axis diffraction setup.

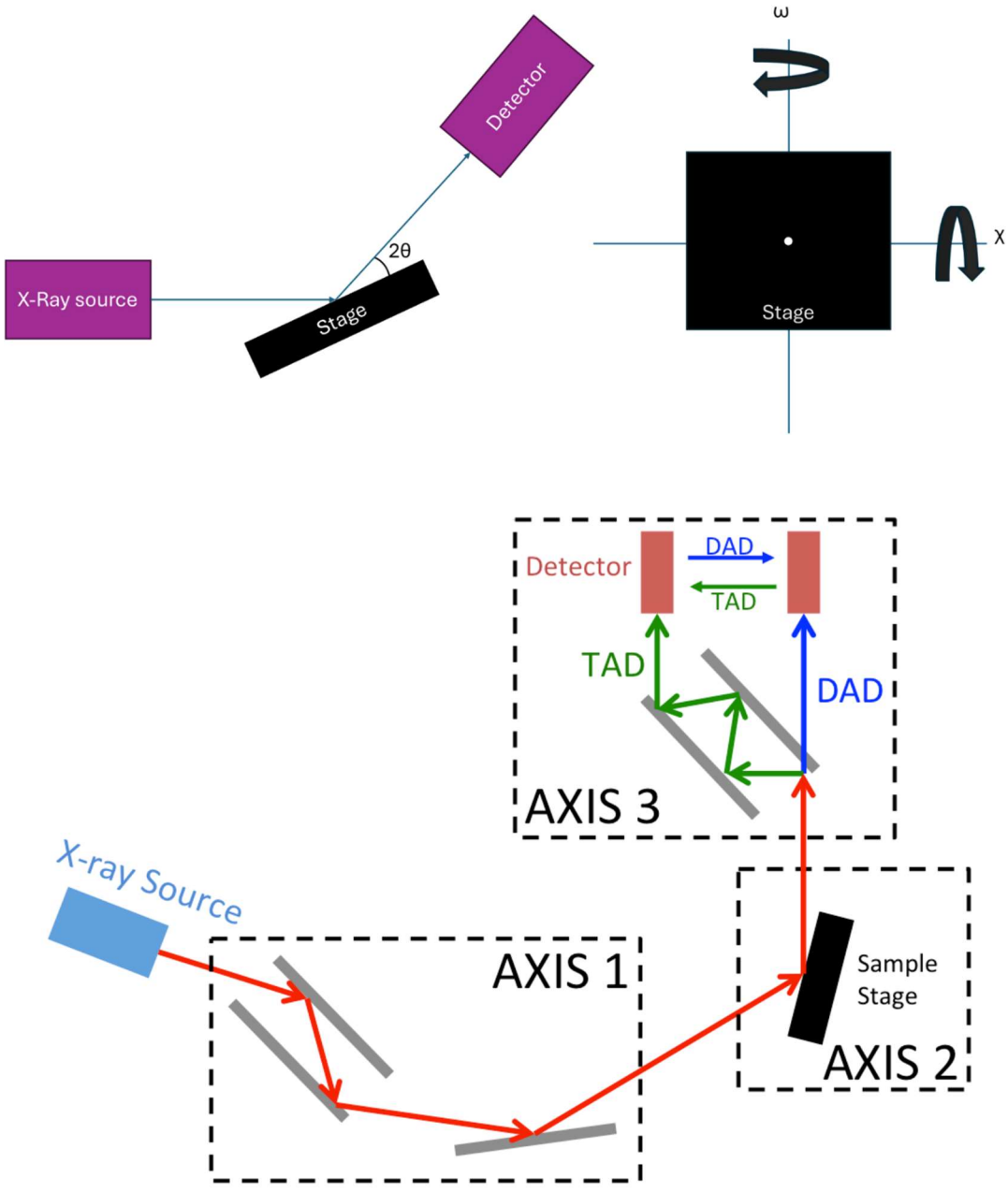

Figure 6: Setup of the XRD equipment [8]

The sample is half cut, that is half of the x-ray beam is inside the sample, this involves positioning the sample in the beam and aligning the ω motor such that half of the x-ray is inside the sample and the sample surface is parallel to the x-ray beam. After half cut, ω and 2θ motors are moved to the diffraction parameters of the (1 0 $\bar{1}$ 4) reflection. This is the symmetric peak for 128Y-cut lithium niobate. Symmetric peaks are reflections of planes that are oriented with the surface plane. For such peaks, the position of the ω motor is exactly half of the 2θ motor. During the preparation of the wafers, the lithium niobate might have been miscut, i.e., the sample surface is slightly offset from the intended (1 0 $\bar{1}$ 4) surface plane. To counteract this, the ω and χ motors are varied together such that maximum intensity is achieved. This ensures that the conditions required for Bragg's diffraction are achieved.

One of the scans performed for this report is a ω-2θ (or θ-2θ) scan. This scan is utilized to measure the lattice spacing of the material which can be used to calculate parameters like composition and strain. As this scan is performed at the symmetric (1 0 $\bar{1}$ 4) reflection, the angle through which the ω motor moves is always at half the value through which the 2θ motor moves. Using Bragg's law, the separation (θ) of the strain peak and the main peak in degrees can be used to calculate the lattice spacing (d) in Å, which is then converted to a strain value in % as shown below:

$$\lambda = 2d \sin \theta \tag{2}$$

$$\text{Strain} = \frac{d - d_0}{d_0} \tag{3}$$

where d_0 is the lattice parameter of pristine lithium niobate.

Another type of XRD scan utilized in this report is a rocking curve. In this, the sample is first oriented to the symmetric (1 0 $\bar{1}$ 4) reflection, after which the sample is rotated using the ω motor. This scan provides information on the distribution of the surface plane as a function of sample tilt (ω). Depending on the mosaicity of the grains, dislocation density or the curvature of the substrate, the parallel nature of the lattice planes vary. As seen in the image below, in the case of the epitaxial thin films grown on a substrate from reference [5], the lattice planes of the substrate (grey) are more "parallel" in comparison to the epi-layer (orange). This leads to a wider rocking curve for the epi-layer as shown in Fig. 7(b). The full width half maximum (FWHM) of the rocking curve is often used to summarize the measurement. A smaller FWHM would indicate a film with better crystalline quality thus offering better device performance.

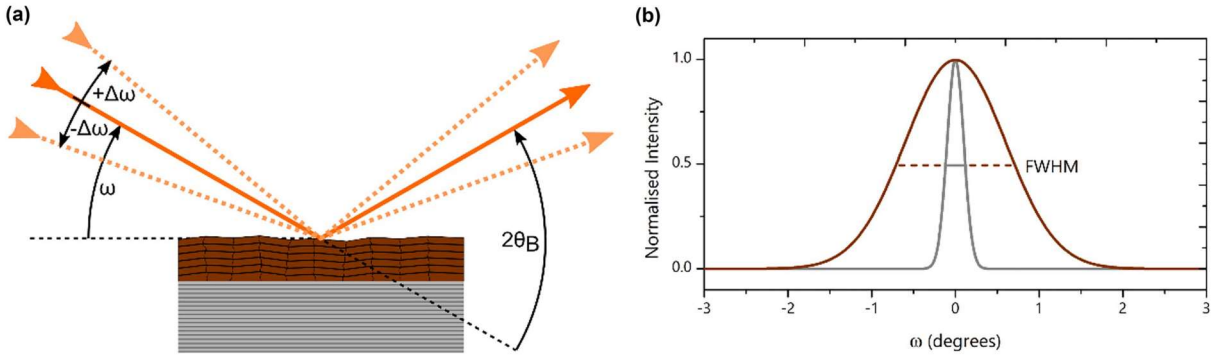

Figure 7: (a) Schematic of a rocking curve measurement and (b) example of rocking curve [5]

Thus, ω-2θ XRD scans will help visualize the strain in lithium niobate implanted with helium, as the implanted helium atoms occupy interstitial positions in the lithium niobate lattice, thus straining it. Strain induced by the implanted helium atoms are resolved better in an ω-2θ scan as it allows a step size in arcsec which is 1/3600 of a degree. An "as-implanted" diffraction pattern of a lithium niobate sample implanted with helium at an energy of 250 keV is shown in Fig. 8.

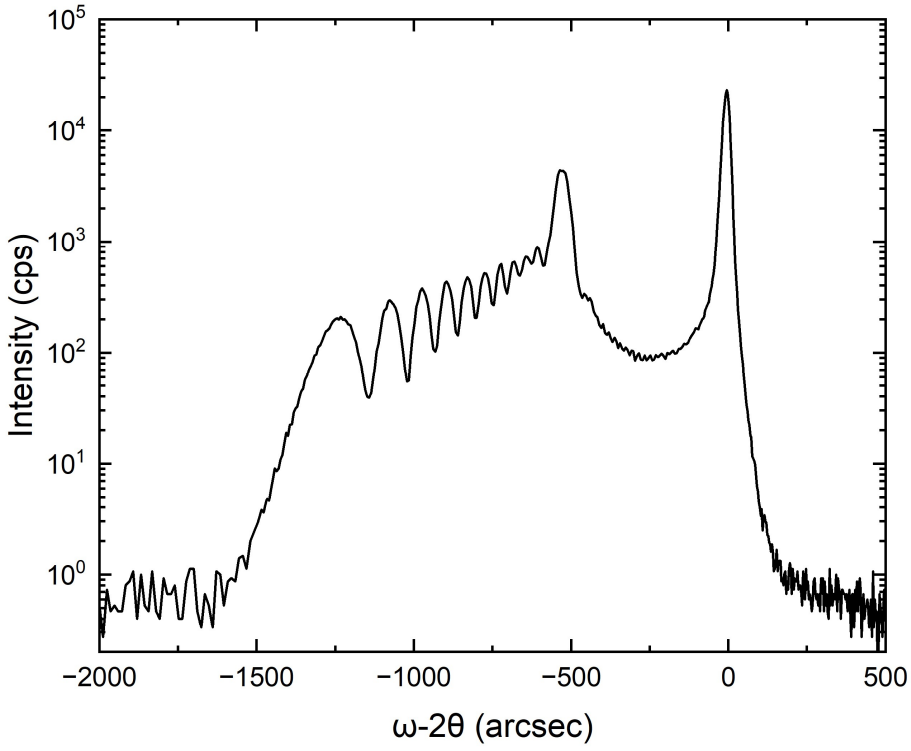

Figure 8: XRD pattern of a 250 keV helium Implanted lithium niobate wafer

As shown in Fig. 1, the implant concentration follows a skewed-gaussian distribution. This results in gaussian fringes in the XRD pattern. The projected range has the highest implant concentration, which corresponds to the maximum implant strain seen at ~ 1200 arcsec. For better understanding, the gaussian relationship between the implant concentration and the depth leads to a monotonically increasing strain till the projected range after which the strain reduces (refer to Fig. 1). This leads to regions in the sample with the same strain value before and after the projected range. These regions with a similar strain diffract at the same value of ω-2θ assuming the composition of the sample remains constant. The separation between the regions with the same strain value produces a phase difference between the x-rays diffracted from the regions, which leads to constructive and destructive interference depending on the separation. The width of the fringes increases as the separation between the similarly strained regions is smaller. For example,

regions possessing the highest strain value are close to each other due to the sharpness of the gaussian distribution. Thus, the fringe corresponding to the highest strain is the widest, while the fringes corresponding to lower strain values are sharper because of a larger separation between the regions with that strain value. For this sample, the maximum implanted strain is calculated as 2.12 %. As the sample is annealed, helium atoms exit the interstitial sites to form helium bubbles via nucleation and ripening as discussed previously. As the bubbles nucleate/grow, the implant induced strain reduces, thus reducing the amplitude of the fringes. As seen in Fig. 9, after exfoliation, most of the implanted helium has left the lithium niobate lattice as indicated by the reduced lattice strain of 0.15 %. This will be explained further in the experimental section of this report.

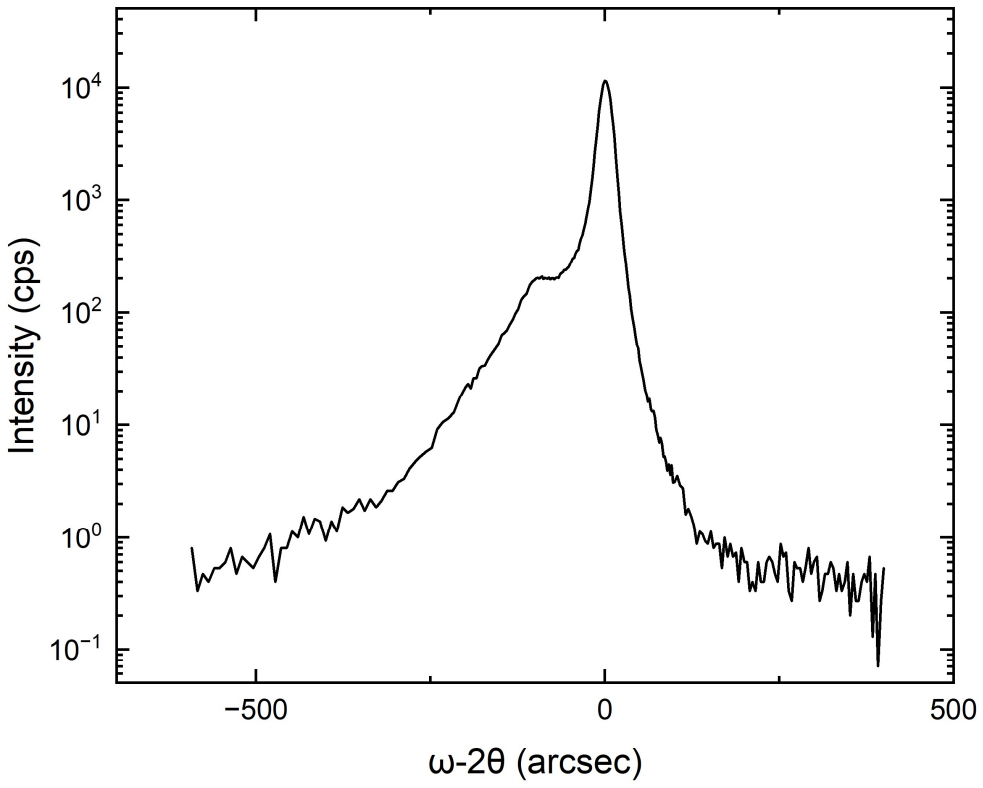

Figure 9: XRD pattern of helium Implanted lithium niobate wafer after exfoliation

Also, XRD rocking curves are utilized to understand how the mosaicity of the substrate changes with the annealing. A rocking curve will offer insights into the crystalline perfection of the implanted substrate. A broad rocking curve would suggest a higher order of imperfections in the lattice. Thus, a sharp rocking curve is crucial for the performance of devices made with the transferred thin films.

3.3: Stylus Profilometry:

In this thesis, a Veeco Dektak 8 Stylus Profilometer (UCLA Nanolab) is used to measure the thickness of the exfoliated thin film, which is the height difference between the exfoliated and non-exfoliated regions in the sample. This measurement helps in verifying that the exfoliation seen in the sample by optical microscopy is due to ion implantation and annealing.

As discussed previously, the thickness of the exfoliated thin film is equal to the projected range of the ion implantation. SRIM simulation of a He^+ ion implantation performed at an implantation energy of 250 keV in a lithium niobate wafer of density 4.647 g/cm^3 at an angle of 7˚ yields a projected range of 800 nm and a straggle of 120 nm. Thus, the expected thickness of the exfoliated thin film is 800 nm.

3.4: Annealing experiments:

The motivation for this work was research performed earlier in the group on the large area exfoliation of indium phosphide using hydrogen-ion implantation which achieved micrometer-scale exfoliation [4]. As discussed previously, at low temperatures, helium bubble nucleation is the dominant process, while at high temperatures, helium diffusion and bubble growth dominates nucleation. Thus, as temperature increases, the bubble size increases while total number of bubbles decreases. For large area exfoliation to occur, a balance between size and number of bubbles is

required. Hence, a two-step annealing experiment is performed where the low temperature "bubble nucleation" anneal is done first before a subsequent high temperature "bubble growth" anneal. A bell-curve relationship exists between the size of the exfoliated region and the temperature at which the nucleation anneal was performed, with the best nucleation anneal having the maximum exfoliated region.

The annealing studies were performed on a Torrey Pines Scientific programmable hotplate. The hotplate was first heated to the setpoint, and the temperature was allowed to stabilize for ~10 minutes. After this, a thermocouple was used to measure the temperature on the hotplate where the sample would be placed. The thermocouple reading was allowed to stabilize for 1 minute before the reading was noted and the sample was placed on the hotplate after confirming that the center of the sample was at the setpoint temperature. After placing the sample, thermocouple readings were taken at 5 points around the sample to quantify the temperature variation across the sample. The thermocouple readings usually varied by ± 3 ˚C.

In the low temperature anneal, the helium bubbles nucleate at the projected range. These bubbles would then grow further in the high temperature step. At a critical point, the pressure of the helium inside the bubble is large enough to cause crack initiation, which then propagates on the surface plane due to proximity of adjacent bubbles. To determine the ideal low-temperature anneal, various low temperature nucleation anneals were first performed, before performing a high temperature anneal at 200 ˚C until blistering/exfoliation is seen on the sample. This is seen as an iridescent green-purple color on the sample at a macroscopic scale. The low temperature annealing steps used were 100 ˚C, 120 ˚C and 140 ˚C. Each annealing lasted a total of 30 hours in increments of 2, 4, 8 and 16 hours. ω-2θ XRD scans were performed on the as-implanted sample and after every annealing step. After the low temperature nucleation annealing, a high temperature bubble

growth anneal at 200 ˚C was performed until exfoliation was seen on the sample when viewed under the optical microscope.

Stylus Profilometry was performed on the sample after the high temperature anneal to confirm that the exfoliated film had a thickness of 800 nm, which would confirm that the exfoliation was caused by the ion implanted helium.

CHAPTER 4: DISCUSSION AND RESULTS

4.1: Optical Microscopy:

As discussed previously, low temperature "nucleation" anneals were performed on the samples at 100 ˚C, 120 ˚C and 145 ˚C. Optical microscopy was performed on the samples to confirm no exfoliation occurred during the low temperature annealing. Subsequently, the samples were annealed at 200 ˚C until exfoliation was seen on the sample. The annealing recipe used for each of the three samples is summarized in Table 1 below. The high temperature anneal at 200 ˚C was performed in steps of 1 hour, 2 hours, 4 hours and 8 hours. It is to be noted that exfoliation happened sometime before the time indicated in the "high temperature anneal" column. For example, sample 1 could have exfoliated anytime between 7 to 15 hours.

Table 1: Annealing recipes used for this study

Sample ID	Low temperature anneal	High temperature anneal
1	100 ˚C 30 hours	200 ˚C 15 h
2	120 ˚C 30 hours	200 ˚C 3 h
3	145 ˚C 14 hours	200 ˚C 3 h

The Nomarski microscopy images of the three samples listed above are shown in Fig. 10 to 12. The grey areas of the image with a darker contrast are regions of the sample which have already exfoliated, while the rest of the sample with a slightly brighter contrast have not exfoliated yet. The white bubbles seen under the surface of the sample are accumulated helium bubbles which are yet to exfoliate. The samples were not cleaned prior to microscopy to prevent any exfoliation occurring during the cleaning process. Hence black particles and ellipse-shaped exfoliated thin

films of 128 Y lithium niobate are seen on the surface of the sample. Also, it is seen that the low temperature annealing for sample 5 lasted only 14 hours (i.e. steps of 2, 4 and 8 hours), while all other samples were annealed for 30 hours (steps of 2, 4, 8 and 16 hours). This is because the XRD pattern after 14 hours of annealing at 145 ˚C indicated a large decrease in the strain in comparison to the other samples indicating that bubble growth was the dominant mechanism. As discussed earlier, low temperature annealing step is performed for bubble nucleation, and it was evident from the XRD scan that 145 ˚C low temperature anneal was not ideal. To confirm, one sample was annealed at 160 ˚C for 2 hours and the XRD scan reported a large decrease in the strain, confirming that bubble growth was the dominant mechanism at 145 and 160 ˚C.

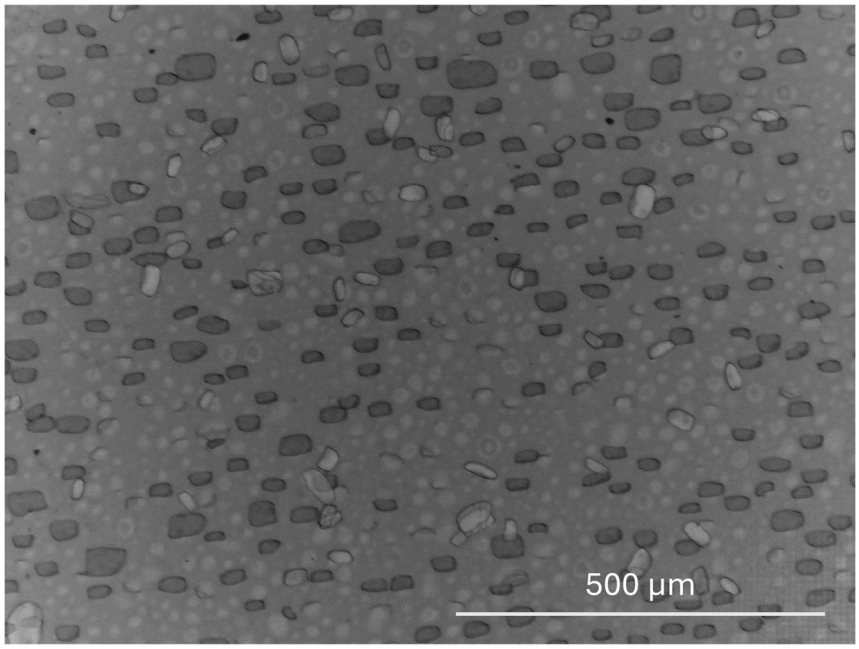

Figure 10: Optical microscope image of sample 1 (100˚C 30h + 200˚C 15h)

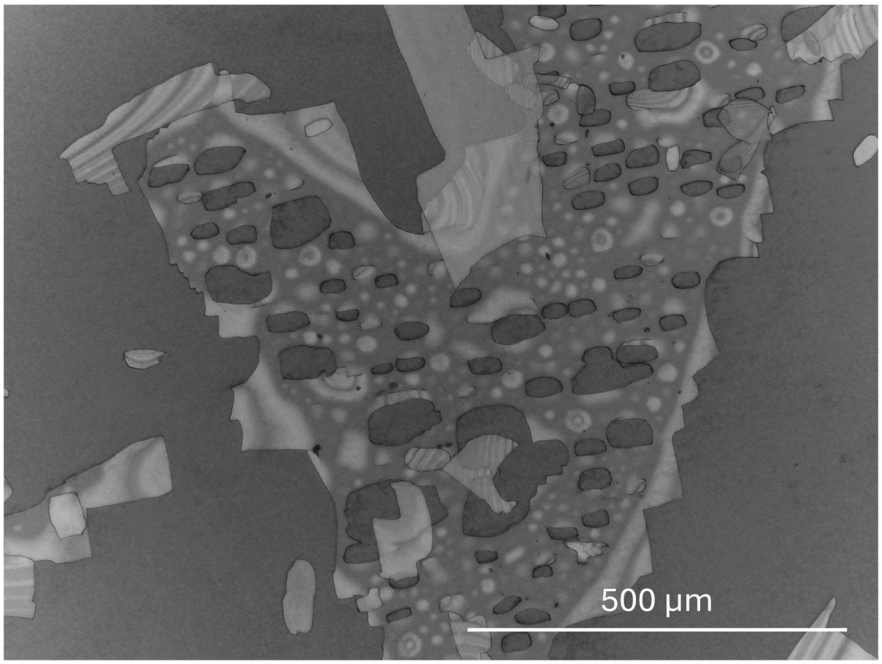

Figure 11: Optical microscope image of sample 2 (120˚C 30h + 200˚C 3h)

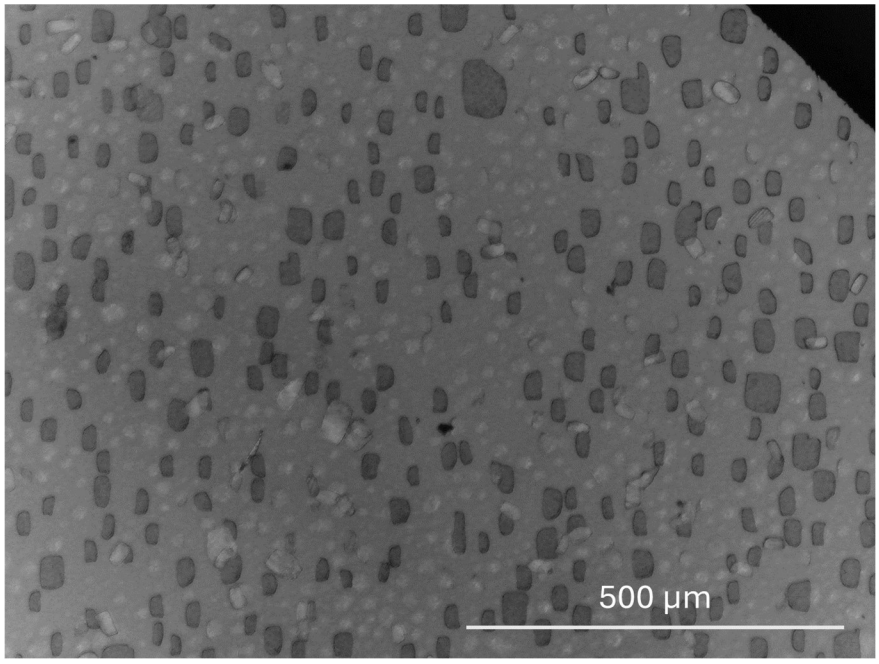

Figure 12: Optical microscope image of sample 3 (145 ˚C 14h + 200˚C 3h)

The percentage exfoliated area with respect to the area of the optical image was measured for each sample. This data is compiled in table 2 below. It is evident that sample 2 has the largest exfoliated area. Fig. 11 shows a sample which had a 120 ˚C 30-hour nucleation anneal prior to a 200 ˚C growth anneal for 3 hours and had large area exfoliation, with the exfoliated area in some regions of the sample being on the scale of millimeters.

Table 2: Area of exfoliation as measured using Adobe Photoshop

Sample ID	Low temperature anneal	High temperature anneal	% Exfoliated area
1	100 ˚C 30 hours	200 ˚C 15 h	13 %
2	120 ˚C 30 hours	200 ˚C 3 h	79 %
3	145 ˚C 14 hours	200 ˚C 3 h	15 %

Notable observations/inferences from the microscope data are:

1. It is evident that the temperature range of the nucleation anneal in which large area exfoliation can be achieved is less than 20 ˚C. This explains why only a small area of the sample achieved large area exfoliation while the rest of the sample had blistering. This is possibly due to temperature variation across the hotplate on which the sample was annealed. During the experiments, the hotplate temperature varied by ± 3 ˚C around the sample, hence limiting the region where a temperature of ~ 120 ˚C was attained. This is supported by the stitched optical microscope image of the entire sample surface shown in Fig. 13. It is seen that most of the top-left quadrant of the sample had large area exfoliation, while area in the bottom-right quadrant of the same sample had blistering. Hence, temperature control during the nucleation anneal is crucial for large area exfoliation.

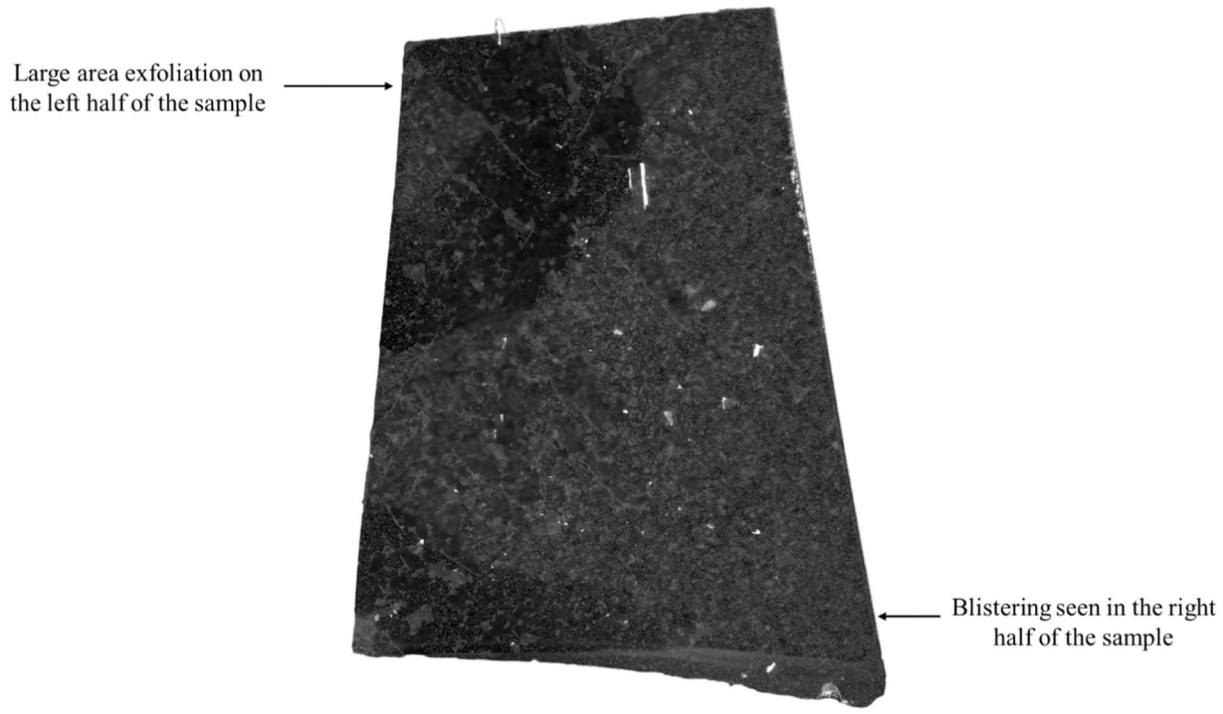

Figure 13: Both Blistering and Large area exfoliation seen in sample 2

4.2: Stylus Profilometry:

The stylus profilometer scan across the exfoliated surface of Sample 2 is shown in Fig. 14 below. The step height measured was measured to be 798 nm, which is equal to the 800 nm exfoliated thickness expected from the SRIM simulations, confirming that the exfoliation was indeed due to the light ion implantation and annealing procedure. There are some height variations seen as indicated by the peaks. These are probably dust particles on the sample surface.

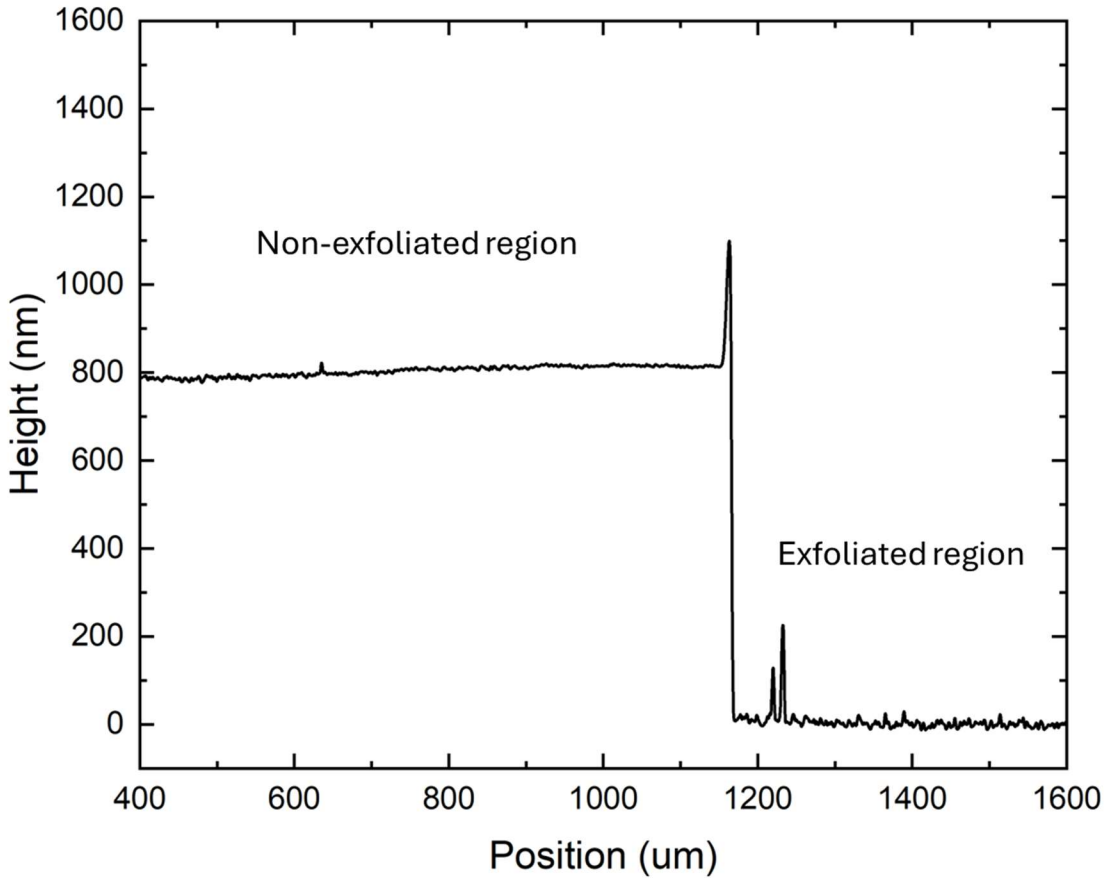

Figure 14: Stylus profilometer scan across the exfoliated region

4.3: XRD analysis and strain measurements:

The surface plane of 128Y cut lithium niobate is (1 0 $\bar{1}$ 4), hence the out-of-plane strain induced by the implantation can be captured in a ω-2θ scan near the symmetric (1 0 $\bar{1}$ 4) reflection. XRD measurements were performed on the as-implanted sample before they were annealed and after each "low temperature" annealing step, the plots for these scans are shown below in Fig. 15-18. Implant induced strain for each XRD pattern is calculated using the interplanar spacing corresponding to the position of the last strain fringe. As discussed earlier, the last strain fringe corresponds to the maximum implant induced strain and gives insights into the evolution of helium bubbles at the projected range. This fringe is indicated by the vertical line in each figure.

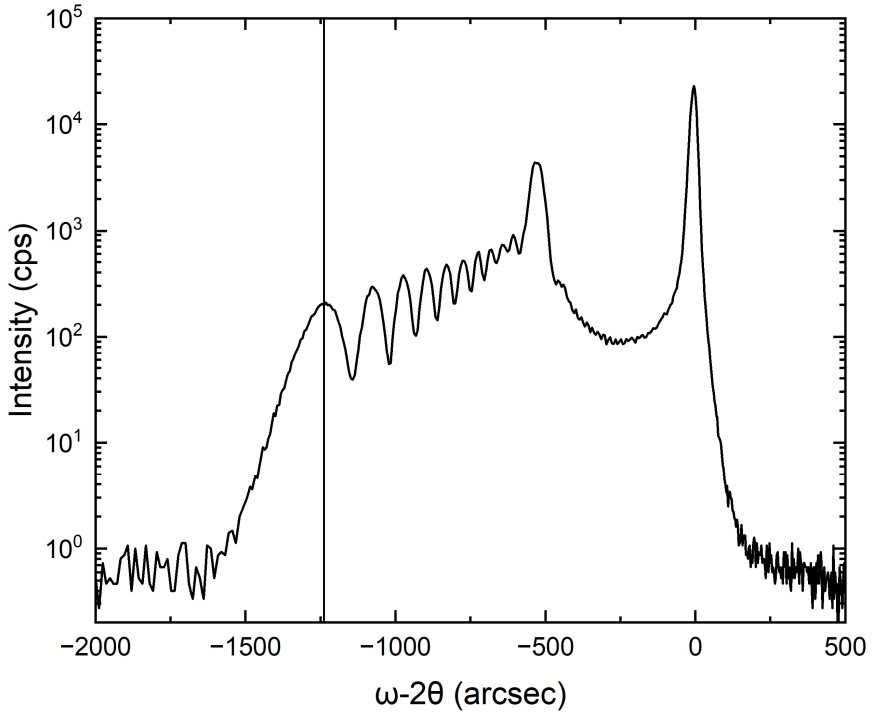

Figure 15: ω-2θ XRD pattern of the as implanted sample

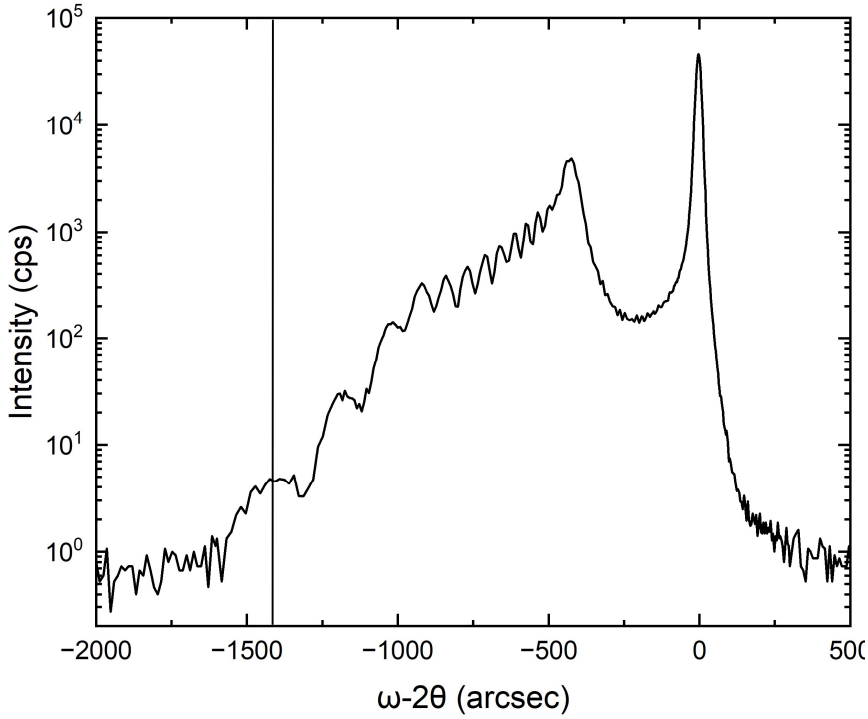

Figure 16: ω-2θ XRD pattern of sample 1 after 100 ˚C for 30 hours

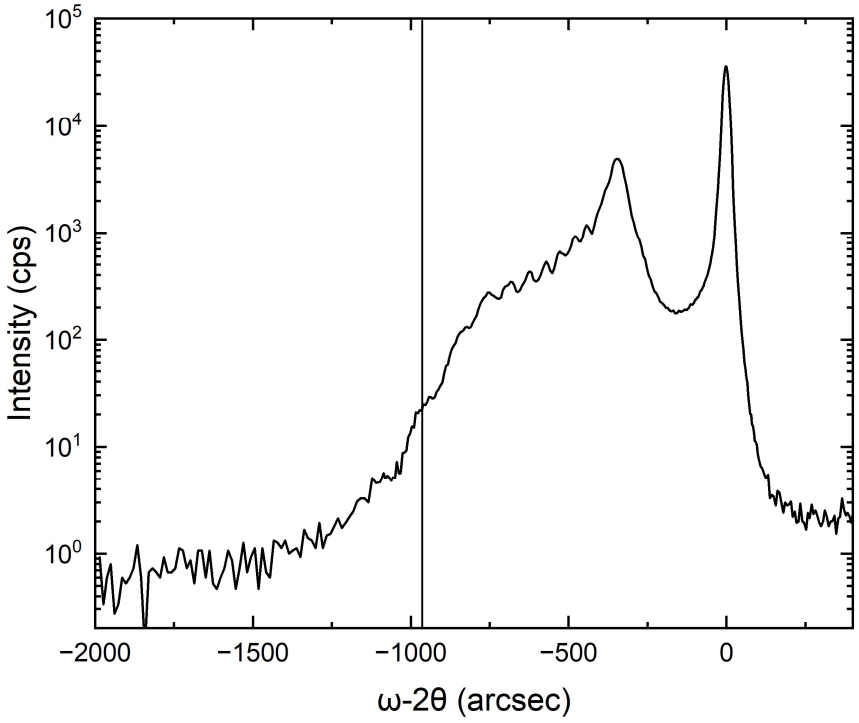

Figure 17: ω-2θ XRD pattern of sample 2 after 120 ˚C for 30 hours

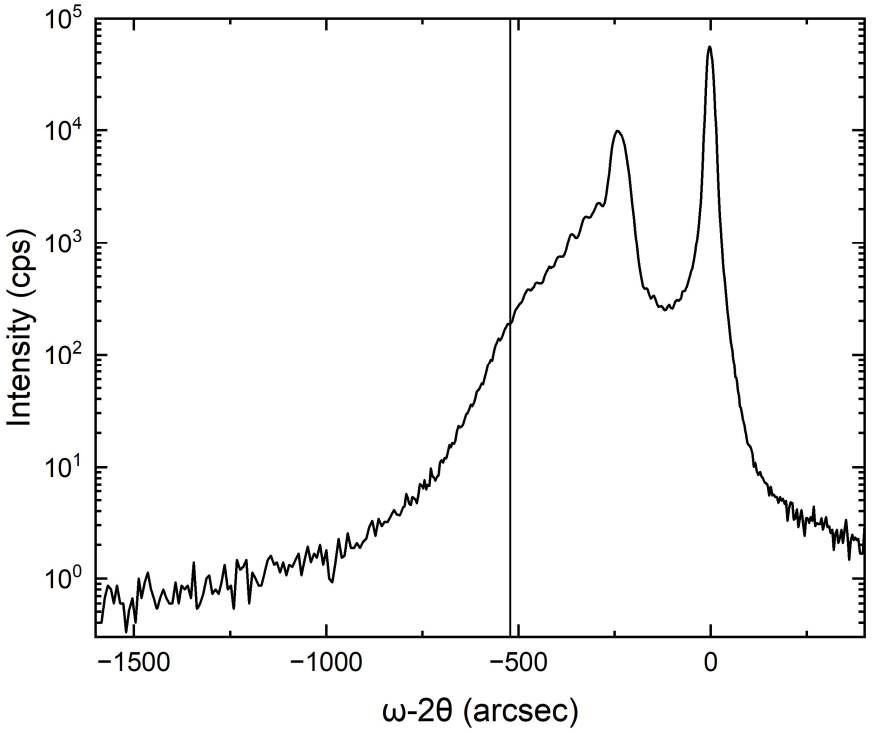

Figure 18: ω-2θ XRD pattern of sample 3 after 145 ˚C for 14 hours

Table 3 below summarizes the maximum implant strain of the samples studied in this report. Although the maximum implant strain increases in sample 1 after the 100 ˚C anneal and there is a general reduction in the implant induced strain as seen by the shift of the strain fringes along the x-axis. Similar reduction in strain is seen in samples 2 and 3 which were annealed at 120 and 145 ˚C respectively.

Table 3: Implant induced strain measured from the XRD fringe pattern

Sample ID	Annealing Recipe	Maximum implant strain (%)
-	Pre-anneal	2.12
1	100 ˚C 30 hours	2.43
2	120 ˚C 30 hours	1.67
3	145 ˚C 14 hours	0.87

As discussed previously in Chapter 4.1, nucleation anneal at 120 ˚C for 30 hours led to large area exfoliation during a 200 ˚C 3 hour anneal. An ω-2θ XRD pattern of the sample after exfoliation is shown in Fig. 19. It is seen that most of the implant induced strain has been removed with a residual strain of 0.15 %. The optical microscope image shown in Fig. 11 and 13 show that the sample both blistering and large area exfoliation in different regions of the sample. Nonetheless, XRD patterns of the blistered and exfoliated regions show a similar strain state.

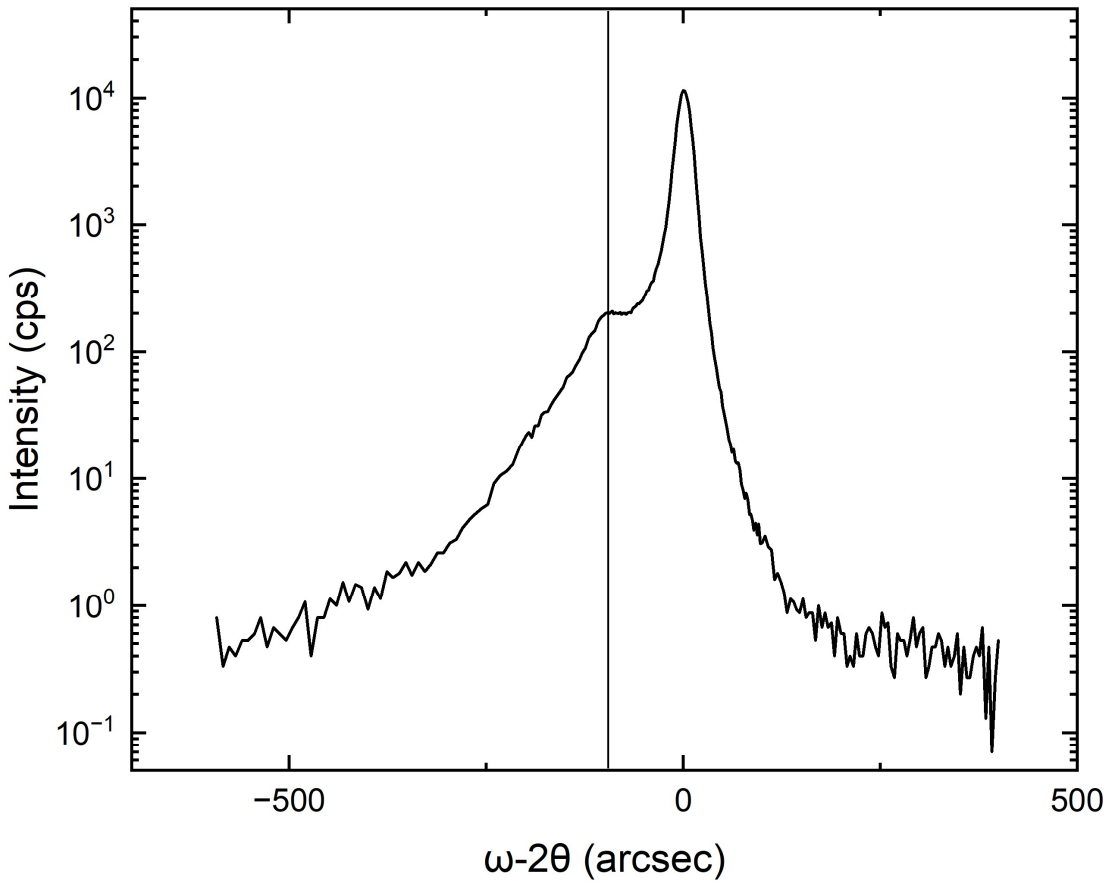

Figure 19: ω-2θ XRD of the exfoliated sample after a 120 ˚C 30 hour + 200 ˚C 3 hour anneal

Further Analysis:

The aim of this thesis project was to evaluate if large area exfoliation could be achieved by varying the annealing recipe after ion implantation. Large area exfoliation of 128Y-cut LN has been achieved previously by increasing the dosage of the ion implantation processes [6], but earlier work in the group which used ion implantation at higher dosage reported an increase in the surface roughness of the as-implanted sample which would reduce the efficiency of the direct wafer bonding step of the Smart Cut technique. As discussed previously, the ω-2θ XRD strain profile can give insights into the concentration vs depth profile of the ion implanted helium.

Another inference that can be made from the XRD data is using the strain fringes. Strain fringes arise from constructive and destructive interference between atoms which are at the same strain value but at different depths as decided by the Gaussian implant concentration vs depth profile shown in Fig. 1. In samples 1 (100 ˚C) and 2 (120 ˚C) (Fig. 16 and 17 respectively), strain fringes at the tail of the XRD profile are prominent, while in sample 3 (145 ˚C) (Fig. 18) there are no strain fringes at the tail of the profile. This can be understood better using Fig. 20. In this figure, parts (a), (b) correspond to the as-implanted sample; (c), (d) correspond to the implanted sample after a 120 ˚C anneal for 30 hours and (e), (f) correspond to an implanted sample after a 145 ˚C 16 hour anneal.

The presence of fringes near the tail of the XRD profile of sample 3 (Fig. 20(c)) indicate symmetry in the concentration profile near the projected range. However, there is a considerable reduction in the intensity of the maximum implanted strain, hinting that helium has nucleated only at the projected range with minimal nucleation at other depths. As all helium nuclei are at the same depth after the nucleation anneal, crack propagation on the 128Y surface plane is easier during the high temperature anneal, thus leading to large area exfoliation. This is supported by large area exfoliation seen in the optical microscope image in Fig. 11.

On the other hand, absence of fringes at the tail of the XRD profile in sample 3 (Fig. 20(e)) indicate that interstitial helium atoms from a wide range of depths has diffused out of the lattice to form helium bubbles. For example, after the 145 ˚C annealing step in sample 3, it seems like helium Nucleation occurred at a wide range of depths, hindering crack propagation along the surface plane, thus leading to blistering. This is supported by the fact that blistering was seen in Fig. 12.

This analysis is qualitative and needs to be confirmed by repeating the study for another orientation of lithium niobate or another material, in which the dominant exfoliation mechanism is blistering. Nonetheless, it seems like XRD strain profile after a low temperature anneal optimized for large area exfoliation would have the following characteristics:

1. Reduction of the intensity of the fringe corresponding to the maximum strain
2. Retention of fringes corresponding to lower strain values at the tail of the XRD pattern (i.e. helium is still present at lattice sites at depths away from the projected range)

It is to be noted that Fig. 20 (d) and (f) are the proposed concentration profiles and is a very simplified approximation. It is made assuming that all helium diffusion occurring during the annealing contribute to the nucleation of helium bubbles at the projected range. Further studies to follow up on this thesis would be to perform simulations of the XRD strain profile for the proposed concentration vs depth profile after the 120 ˚C and 145 ˚C anneal and check if it matches the measured XRD profiles shown in the Fig. 20. If the simulation matches the measurement, it will confirm that an “optimized” low temperature annealing should reduce the amplitude of the strain fringe corresponding to the maximum implanted strain while not affecting the amplitude of other strain fringes corresponding to lower strain values.

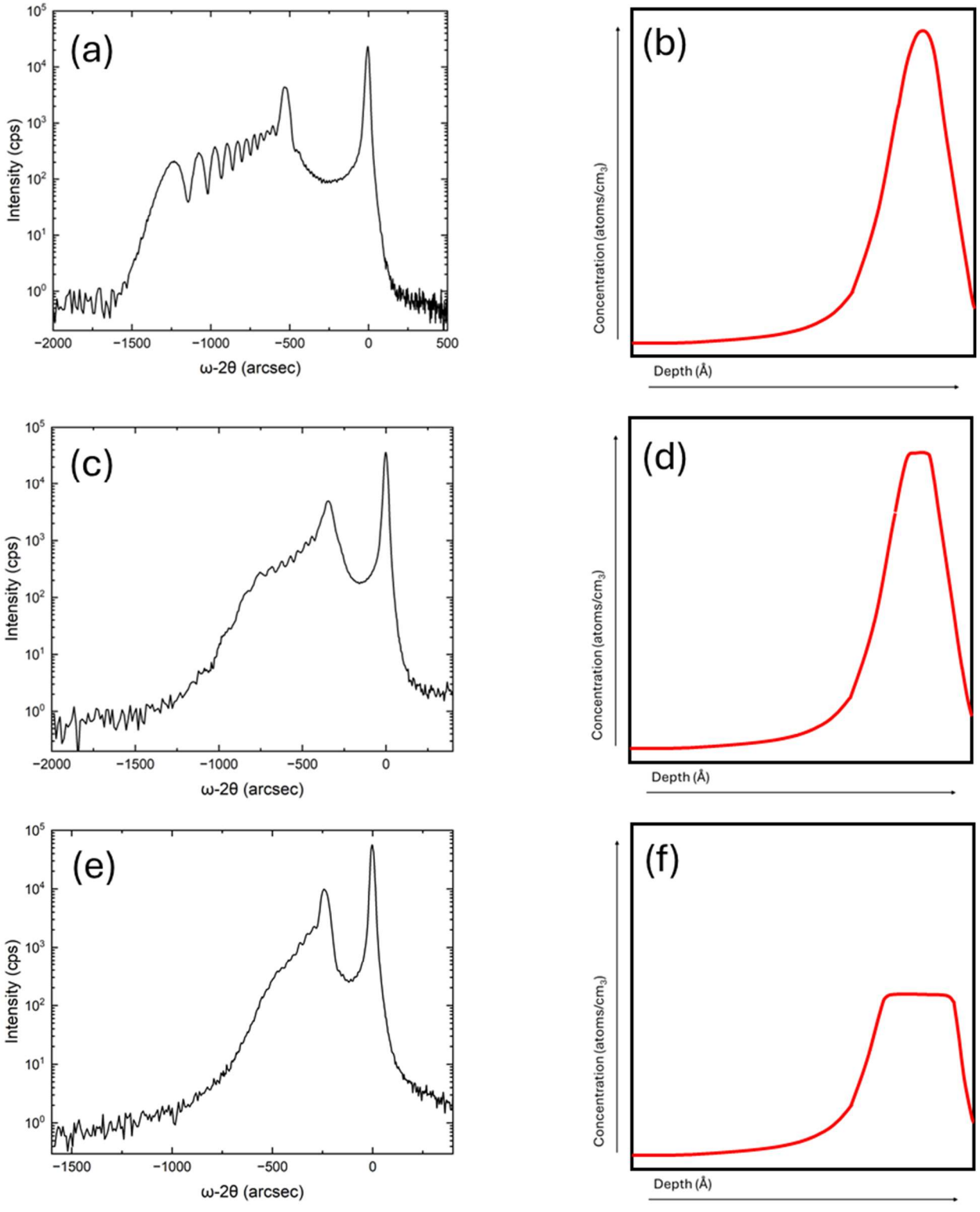

Figure 20: ω-2θ XRD pattern and concentration vs depth profiles of (a, b) as-implanted sample (c, d) after 120 ˚C - 30 hours annealing and (e, f) after 145 ˚C - 16 hours annealing

CHAPTER 5: CONCLUSION

In this thesis, the annealing recipe of the light ion exfoliation technique for the heterogeneous integration of thin film lithium niobate using helium ion implantation has been investigated. lithium niobate wafers were ion-implanted with helium ions at an implant voltage 250 keV and a dosage of $2.3x10^{16}$ ions/cm^2. A low temperature anneal was used as a nucleation step to enable efficient large area exfoliation of lithium niobate during the subsequent high temperature "growth" anneal. The annealing recipe which led to the largest exfoliated area was a low temperature anneal at 120 ˚C for 30 hours followed by annealing at 200 ˚C for 3 hours. It is to be noted that the temperatures required for large-area exfoliation will vary depending on the annealing equipment and the implantation. For example, the hotplate used in these annealing studies had a temperature variation of roughly ±3 ˚C across the sample and needs to be accounted for. Also, the straggle of the implant concentration profile will affect the exfoliation, as it directly correlates to the amount of helium available to cause bubble growth. Thus, large area exfoliation might be difficult to achieve with implants performed at a low accelerating voltage due to the low straggle. Although, this hypothesis has not been confirmed yet. To conclude, large area exfoliation of the 128Y-cut orientation of lithium niobate has been previously reported by changing the dosage of the ion implantation [6]. But increasing the ion implantation dose increases implantation induced damage which leads to an increase in the surface roughness of the implanted wafer making it unsuitable for direct wafer bonding. This work serves as proof of concept that such large area exfoliation can be achieved by tuning the annealing recipe without changing the implantation parameters.

REFERENCES

[1] L. Matto, et al., “Thin Film Layer Transfer of 128° Y-cut LiNbO3 on (0001) Al2O3 Through Ion Implantation and Exfoliation,” Oral Presentation, Electronic Materials Conference 2023 (2023)

[2] Weis, R. S., & Gaylord, T. K. (1985). lithium niobate: Summary of Physical Properties and Crystal Structure. In Appl. Phys. A (Vol. 37).

[3] James F. Ziegler et al, SRIM – The stopping and range of ions in matter (2010), Nuclear Instruments and Methods in Physics Research Section B: Beam Interactions with Materials and Atoms, Volume 268, Issues 11–12, 2010, Pages 1818-1823

[4] Hayashi, S., Bruno, D., & Goorsky, M. S. (2004). Temperature dependence of hydrogen-induced exfoliation of InP. Applied Physics Letters, 85(2), 236–238

[5] G. F. Harrington and J. Santiso, “Back-to-Basics tutorial: X-ray diffraction of thin films,” J. Electroceramics, vol. 47, no. 4, pp. 141–163, 2021, doi: 10.1007/s10832- 021-00263-6

[6] Ma, R., Liu, W., Sun, X., & Zhou, S. (2021). In-Situ Process and Simulation of High-Performance Piezoelectric-on-Silicon Substrate for SAW Sensor. *Frontiers in Materials*, *8*. https://doi.org/10.3389/fmats.2021.678658

[7] De, R. R. L., Albuquerque, D. A. C., Cruz, T. G. S., Yamaji, F. M., & Leite, F. L. (2012). Measurement of the Nanoscale Roughness by Atomic Force Microscopy: Basic Principles and Applications. In *Atomic Force Microscopy - Imaging, Measuring and Manipulating Surfaces at the Atomic Scale*. InTech. https://doi.org/10.5772/37583

[8] M. E. Liao, “Cadmium Telluride and Grain Boundaries: A Preliminary Study,” University of California, Los Angeles PP - United States -- California, United States -- California, 2017

[9] M. Bruel, "silicon on insulator material technology," Electron. Lett. 31(14), 1201–1202 (1995)